International Journal of Heat and Mass Transfer 75 (2014) 313–326

Contents lists available at ScienceDirect

International Journal of Heat and Mass Transfer

journal homepage: www.elsevier.com/locate/ijhmt

Analysis of non-uniform heat loads on evaporators with loop heat pipes

Tao Fang [a], Tingzhen Ming [a,b,*], C.P. Tso [c], Xiaoming Huang [a], Wei Liu [a]

[a] School of Energy & Power Engineering, Huazhong University of Science and Technology, Wuhan 430074, China
[b] Mechanical & Aerospace Engineering, University of Florida, Gainesville, FL 32611, USA
[c] School of Mechanical & Aerospace Engineering, Nanyang Technological University, 639798 Singapore, Singapore

ARTICLE INFO

Article history:
Received 23 January 2013
Received in revised form 29 August 2013
Accepted 22 March 2014
Available online 24 April 2014

Keywords:
Non-uniform heat load
Evaporation heat transfer
Surface temperature
Flat-plate evaporator
Loop heat pipe

ABSTRACT

Loop heat pipes (LHPs) are passive two-phase heat transfer devices which are widely used in cooling applications such as spacecraft thermal control and electronics cooling. As these devices often encounter non-uniform heat load during operation, a numerical analysis based on a 2-dimensional dynamic mesh model is conducted to gauge the influence of non-uniform load on the performance of a flat-plate evaporator used in LHPs. The variations of evaporation heat transfer coefficient, outflow working fluid temperature, vapor and liquid interface position as well as surface temperature with heat load concentration are analyzed. The results reveal that when the heat load is not highly concentrated and relatively low, non-uniformity facilitates the heat transfer. On the other hand, highly non-uniform heat load will deteriorate heat transfer. Furthermore, the maximum surface temperature will increase significantly under non-uniform heat flux, although the phenomenon can be mitigated by using shell materials with higher heat conductivity.

1. Introduction

Capillary pumped loops (CPLs) and loop heat pipes (LHPs) are similar two-phase heat transfer devices that operate on closed evaporation and condensation cycles, relying on phase transition and capillary pressure to maintain the operation. The first CPL was developed by Stenger in the 1960s [1], while LHPs were invented in Russia in the 1970s [2]. Compared with traditional heat transfer devices such as conduction or air convection cooling systems, CPLs and LHPs are superior in that much higher heat transfer coefficient are obtainable while providing lower surface temperature and temperature differences. Secondly, longer distance and high amount heat transfer are achievable. Therefore, they are wildly used in thermal management systems such as those employed in spacecraft [3] and laptop computers [4].

An evaporator which connects with heating surface directly and provides capillary pressure for the cycle is an important component of LHPs. Some experimental results had been reported in evaporator optimal design [5–8], while Udell [9] showed that within the porous medium there are three different zone, vapor, liquid and two-phase, and the size of two-phase zone could be a function of working fluid and porous media characteristics. Zhao and Liao et al. [10] investigated experimentally the evaporation mechanism within the porous wick and found that under minor heat flux, the porous medium region is saturated, except a few regions near the heating surface. With increasing heat flux, an increasing two-phase zone appears in the top region of the wick. As long as the heat flux exceeds a threshold value, a vapor zone will also appear.

Unfortunately, numerical simulations of the phase transition and heat transfer in evaporator are rather complicated. In the actual situation, LHPs will display an oscillating behavior [11–13] rather than a steady-state one, so that it is not easy to present a conjugate model. Cao and Faghri [14] developed an analytical solution based on a simple model of heat and mass transfer with a liquid-saturated porous wick. Later the same authors [15] used an improved model that coupled vapor groove and porous wick, but assumed that evaporation only occurs in the interface between groove and capillary wick. Demidov and Yatsenko [16] simulated the evaporation process in a capillary structure, and found that at low load the evaporation occurs at the capillary wick and heating wall interface. At higher heat loads, the liquid–vapor interface moves into the capillary structure. Figus et al. [17] also found that the size of the vapor zone is not a simple function of the heat load. Thus, we can expect significant and interesting evaporative heat transfer coefficient variation with increasing heat load.

Recent investigations concentrated in three aspects. The first one is studying new type porous wicks [18–22], Xu et al. [18]

* Corresponding author at: School of Energy & Power Engineering, Huazhong University of Science and Technology, Wuhan 430074, China. Tel.: +86 27 87542618.
E-mail address: tzming@mail.hust.edu.cn (T. Ming).

http://dx.doi.org/10.1016/j.ijheatmasstransfer.2014.03.061
0017-9310/

Nomenclature

Latin symbols

A_t	the area of heating surface, m^2
c	specific heat, $J\ K^{-1}\ kg^{-1}$
C_2	inertial resistance factor, m^{-1}
C_{evap}	thermal conductivity from heating surface to the interface of wick and shell, $W\ m^{-1}\ K^{-1}$
D_p	the porous radius of capillary wick, m
e	natural constants
H_{evap}	evaporative heat transfer coefficient, $W\ m^2\ K^{-1}$
h_f	convection heat transfer coefficient, $W\ m^2\ K^{-1}$
$\vec{V}$	surface normal vector
p	pressure, Pa
p_c	capillary pressure, Pa
$q(x)$	head load function
q_{load}	average heat flux on heating surface, $W\ m^{-2}$
Q_{load}	heat load, W
S	additional momentum source, $kg\ m^{-1}$
t	time, s
T	temperature, K
$\vec{V}$	the vector of velocity, $m\ s^{-1}$
x, y	Cartesian space coordinates

Greek symbols

α	permeability, m^2
γ	heat concentration degree
ε	wick porosity
θ	contact angle, rad
ρ	density, $kg\ m^{-3}$
λ	thermal conductivity, $W\ m^{-1}\ K^{-1}$
μ	dynamic viscosity, $N\ m^{-2}\ s$
σ	mean square deviation
π	Pi
τ	surface tension of working fluid, $N\ m^{-1}$

Subscripts

eff	effective value
evap	evaporation
in	inlet
i	interface between liquid and gas
l	liquid phase
max	maximum value
min	minimum value
outf	outflow
out	outlet
sat	saturated
sh	shell
v	gas phase
wick	porous wick

and Xin et al. [21] studied sintered wicks. Wu et al. [19] and Deng et al. [22] investigated composite wicks. And the work by Lin et al. [20] mainly focused on bidisperse wick. The second is the performance of variety of new structure design evaporator [23–27]. The last is LHP's performance under low temperature [28–30]. These researches are conducted mainly by Bai et al. [29] and Zhao et al. [30].

However, almost all of the experiments and simulations surveyed were conducted with uniform heat fluxes being imposed upon the heating surfaces. While in applications, especially for small-scale flat-plate evaporators, LHPs need to confront with non-uniform heat flux. For example, it is common to use a single evaporator for the cooling of a few close electronic components; and even for a single component, the heat flux will be non-uniform due to the indispensable encapsulation shell which could be much larger than its inner component. Therefore, we report here an investigation on the performance of an evaporator under non-uniform heat flux with numerical simulation method of a dynamic mesh model by using the software FLUENT 14.0, within the commercial software ANSYS 14.0. The model coupled liquid–gas interface moving, phase change, heat and mass transfer rather than merely based on given interface position.

2. The evaporator

2.1. Geometric model

Based on the models of Muraoka et al. [30] and Wan et al. [31,32], a flat-plate type loop heat pipe evaporator is adopted for the numerical simulation, in this paper. In order to limit side metallic wall evaporation, which is unfavorable to the steady operation of the evaporator [31,32], the vapor groove position was modified. As shown in Fig. 1, the size of the evaporator is 43 mm × 10 mm; the wick inside is 37 mm × 4 mm; as for vapor and liquid grooves, it is 1 mm × 1 mm. There are 19 vapor grooves and 18 liquid grooves at the top and the bottom of the porous wick, respectively. In the simulation, the x-axis is aligned in the length direction which ranges from −21.5 mm to 21.5 mm; while the y-axis is in along the width ranging from −5 mm to 5 mm. Regions 1, 2, 3, 4 are evaporator shell, vapor groove, porous wick and liquid groove, respectively. The heating surface is aligned at the top of evaporator and ranges from −18.5 mm to 18.5 mm: the same as the length of porous wick. We assume the surrounding walls as adiabatic.

In the 2-D simulation of inflow and outflow, the inlet and outlet are set as squares, with size 0.4 mm by 0.4 mm, in the center of every groove. The material of both the shell and wick is steel. The pore diameter of the steel wire for the evaporator porous wick is 25 μm. Methyl-alcohol is adopted as the working fluid. The geometric parameters are summarized in Table 1.

2.2. Mathematical model

The mathematical model is based on the following main assumptions: (1) zero gravity effect in space applications, and negligible gravity effect when compared with capillary pressure; (2) the capillary wick is isotropic; (3) the fluid, both vapor and liquid, in wick, grooves and evaporator shell are in thermal equilibrium; (4) the variance of saturation temperature is negligible [33] because the pressure drop in the evaporator is much smaller than the absolute pressure; (5) radiation and convection heat transfers are neglected when compared with conductive and latent heat transfers; (6) fluid flow within the evaporator is laminar, as flow velocity and viscosity influence are small; (7) both liquid and gas phases are incompressible, since incompressibility assumption has borne up well with reported work in this area [14–17]. Based on the above assumptions, the mathematical model under steady state condition in each part of the evaporator are as follows.

2.2.1. Evaporator shell

Energy equation:

$$\lambda_{sh}\left(\frac{\partial^2 T}{\partial x^2}+\frac{\partial^2 T}{\partial y^2}\right)=0. \tag{1}$$

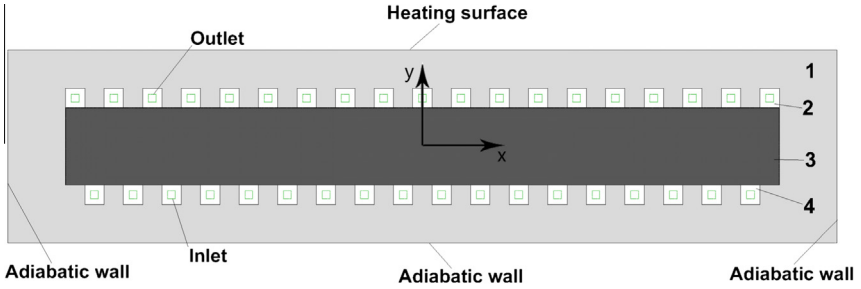

Fig. 1. 2-D geometrical model of the evaporation.

Table 1
The geometric parameters of the evaporator.

Evaporator body	
Length (mm)	43
Width (mm)	10
Material	Steel
Porous wick	
Length (mm)	37
Width (mm)	4
Material	Steel
Pores (μm)	25
Porosity	0.611
Groove	
Length (mm)	1
Width (mm)	1

2.2.2. Vapor in grooves

Energy equation:

$$\lambda_v\left(\frac{\partial^2 T}{\partial x^2}+\frac{\partial^2 T}{\partial y^2}\right)=0. \tag{2}$$

2.2.3. Liquid in grooves

Energy equation:

$$\lambda_l\left(\frac{\partial^2 T}{\partial x^2}+\frac{\partial^2 T}{\partial y^2}\right)=0. \tag{3}$$

2.2.4. Capillary porous wick

Liquid phase continuity equation:

$$\frac{\partial \rho_l V_{l,x}}{\partial x}+\frac{\partial \rho_l V_{l,y}}{\partial y}=0. \tag{4}$$

Liquid phase momentum equations:

$$\frac{\rho_l}{\varepsilon^2}\left(V_{l,x}\frac{\partial V_{l,x}}{\partial x}+V_{l,y}\frac{\partial V_{l,x}}{\partial y}\right)=-\frac{\partial p}{\partial x}+\left(\frac{1}{\varepsilon}\frac{\partial^2 \mu_l}{\partial x^2}+S_{l,x}\right)V_{l,x}, \tag{5}$$

$$\frac{\rho_l}{\varepsilon^2}\left(V_{l,x}\frac{\partial V_{l,y}}{\partial x}+V_{l,y}\frac{\partial V_{l,y}}{\partial y}\right)=-\frac{\partial p}{\partial y}+\left(\frac{1}{\varepsilon}\frac{\partial^2 \mu_l}{\partial y^2}+S_{l,y}\right)V_{l,y}. \tag{6}$$

Liquid phase energy equation:

$$\rho_l c_l\left(\frac{\partial V_{l,x}}{\partial x}+\frac{\partial V_{l,y}}{\partial y}\right)T=(\lambda_{\text{eff}})_l\cdot\frac{\partial^2 T}{\partial x^2}+\frac{\partial^2 T}{\partial y^2}. \tag{7}$$

Gas phase continuity equation:

$$\frac{\partial \rho_v V_{v,x}}{\partial x}+\frac{\partial \rho_v V_{v,y}}{\partial y}=0. \tag{8}$$

Gas phase momentum equations:

$$\frac{\rho_v}{\varepsilon^2}\left(V_{v,x}\frac{\partial V_{v,x}}{\partial x}+V_{v,y}\frac{\partial V_{v,x}}{\partial y}\right)=-\frac{\partial p}{\partial x}+\left(\frac{1}{\varepsilon}\frac{\partial^2 \mu_v}{\partial x^2}+S_{v,x}\right)V_{v,x}, \tag{9}$$

$$\frac{\rho_v}{\varepsilon^2}\left(V_{v,x}\frac{\partial V_{v,y}}{\partial x}+V_{v,y}\frac{\partial V_{v,y}}{\partial y}\right)=-\frac{\partial p}{\partial y}+\left(\frac{1}{\varepsilon}\frac{\partial^2 \mu_v}{\partial y^2}+S_{v,y}\right)V_{v,y}. \tag{10}$$

Gas phase energy equation:

$$\rho_v c_v\left(\frac{\partial V_{v,x}}{\partial x}+\frac{\partial V_{v,y}}{\partial y}\right)T=(\lambda_{\text{eff}})_v\cdot\frac{\partial^2 T}{\partial x^2}+\frac{\partial^2 T}{\partial y^2}. \tag{11}$$

In the above, ε is the porosity of the porous wick which is set as 0.611 in this work. λ_{eff} is effective heat transfer coefficient, defined respectively for the liquid and the vapor as:

$$(\lambda_{\text{eff}})_l=\lambda_l\varepsilon+\lambda_{\text{wick}}(1-\varepsilon), \tag{12}$$

$$(\lambda_{\text{eff}})_v=\lambda_v\varepsilon+\lambda_{\text{wick}}(1-\varepsilon). \tag{13}$$

The λ_{wick} is the thermal conductivity of wick material (steel) and $\lambda_{\text{wick}}=0.2022$ W/m K. The S_l and S_v are additional momentum source terms for the liquid and gas phase, respectively:

$$S_x=-\left(\frac{\mu}{\alpha}V_x+C_2\cdot\frac{1}{2}\rho V\cdot V_x\right), \tag{14}$$

$$S_x=-\left(\frac{\mu}{\alpha}V_y+C_2\cdot\frac{1}{2}\rho V\cdot V_y\right). \tag{15}$$

The first terms on the right-hand side of Eqs. (12) and (13) are Darcy's law terms (which could be regarded as 0 under laminar flow condition) and the second terms are the inertial loss terms. And μ is the viscosity coefficient of the fluid, α and C_2 are the permeability and inertial resistance factor of the porous media, respectively given by [34]:

$$\alpha=\frac{D_p^2}{150}\frac{\varepsilon^3}{(1-\varepsilon)^2}, \tag{16}$$

$$C_2=\frac{3.5}{D_p}\frac{(1-\varepsilon)}{\varepsilon^3}, \tag{17}$$

where D_p is the average diameter of the porous material.

2.3. Boundary condition

2.3.1. At a heating surface

Energy equation:

$$\lambda_{sh}\frac{\partial T}{\partial y}=q(x), \tag{18}$$

where $q(x)$ is a function of heating surface. In order to limit side metallic wall evaporation, which is unfavorable to the steady operation of the evaporator [31,32], the size of the heating area is

the same as the porous wick upper surface (-18.5 mm < x < 18.5 mm). The normal distribution function is used to represent the heat concentration along the heat area:

$$q(x) = \frac{P}{\sqrt{2\pi}\sigma} e^{-\frac{(x-x_c)^2}{2\sigma^2}} \quad (-18.5\ \text{mm} \le x \le 18.5\ \text{mm}), \tag{19}$$

$$q(x) = 0 \quad (x < -18.5\ \text{mm} \ \text{ and } \ x > 18.5\ \text{mm}). \tag{20}$$

In the above equations, σ is the root mean square deviation which can represent different concentrations of heat flux imposed upon the wall.

In this paper, the value $\gamma = 0.0185/\sigma$ is adopted to represent the degree of heat concentration, the higher the greater the heat load. And x_c is the heating center which is also the point with maximum heat flux. P is a coefficient that represents the heating power, that needs to be calculated for each overall power, for a given σ and x_c. Although an infinite σ can describe a uniform heat flux, it is not convenient to be dealt with in FLUENT UDF. Thus we will replace Eq. (19) with a square wave function:

$$q(x) = q_{\text{load}} \quad (-18.5\ \text{mm} \le x \le 18.5\ \text{mm}), \tag{21}$$

$$q(x) = 0, (x < -18.5\ \text{mm} \ \text{ and } \ x > 18.5\ \text{mm}), \tag{22}$$

where q_{load} is the average heat flux on heating surface.

2.3.2. At an adiabatic surface

Energy equation:

$$\lambda_{sh} \frac{\partial T}{\partial x} = 0. \tag{23}$$

The reason for setting the other outer surfaces of the shell (the non-heating surfaces) as adiabatic is because we are focusing on the evaporator performance under non-uniform heat flux working condition at the heating surface, and wish to exclude other influences.

2.3.3. At the inlet

We set pressure as the inlet condition (the gauge pressure):

$$p_{\text{in}} = 0Pa. \tag{24}$$

2.3.4. At the outlet

The outlet is also set by pressure.

$$p_{\text{out}} = 0Pa. \tag{25}$$

The operating pressure is 27.863 kPa which is also the saturated pressure of methyl-alcohol at 308 K. In fact, the pressure at the inlet and outlet of the evaporator are not the same because of pressure head loss in the fluid flow. Under extremely low temperature and small heat load, the system will encounter a viscous limit [35]. But here, under high heat load, the pressure head loss can be neglected comparing with capillary pressure. Furthermore, we only focus on the isolated evaporator, so that the pressure difference between the inlet and outlet has little influence on the results.

2.3.5. The interface of vapor and liquid in capillary wick

During operation, although there is a pressure difference at the vapor–liquid interface, the pressure can reach an equilibrium because of the capillary effect. However, when the pressure difference exceeds certain limit, the interface will move.

Heat flux continuity:

$$(\lambda_{\text{eff}})_v \left(\frac{\partial T_v}{\partial x} + \frac{\partial T_v}{\partial y}\right) \cdot \vec{n} - (\lambda_{\text{eff}})_l \left(\frac{\partial T_l}{\partial x} + \frac{\partial T_l}{\partial y}\right) \cdot \vec{n} = \rho_l h_f V_l, \tag{26}$$

where $\vec{n}$ is the normal unit vector at the interface.

Mass continuity:

$$\rho_v V_{v,x} = \rho_l V_{l,x}, \tag{27}$$

$$\rho_v V_{v,y} = \rho_l V_{l,y}, \tag{28}$$

Pressure balance in quasi-steady condition (strictly speaking, an LHP will never reach a real steady condition in operation [11–13]) is

$$p_v + p_l = p_c, \tag{29}$$

where P_c is the capillary pressure in the porous wick and it is given by the Laplace–Young equation

$$p_c = \frac{4\tau \cos\theta}{D_p}, \tag{30}$$

where τ is the surface tension coefficient of the working fluid. θ is the contact angle.

2.4. Evaporative heat transfer coefficient

Since an evaporator is constituted by shell and wick, the design of its parts, including the geometry and materials of wick and shell, will affect its performance [6–8]. Therefore, average values of evaporative heat transfer coefficient should not be used. Here we use the expression proven to be effective for evaporator performance [36]:

$$H_{\text{evap}} = \frac{1}{\frac{A_t (T_{\text{evap}} - T_{\text{sat}})}{Q_{\text{load}}} - \frac{A_t}{C_{\text{evap}}}}, \tag{31}$$

where T_{evap} is the mean temperature of the evaporator heating surface. T_{sat} is the saturation temperature of the working fluid. Q_{load} is the heat load adopted in the heating surface, and A_t is the area of heating surface. As for C_{evap}, it is the thermal conductance from the heating surface of the evaporator to the interface of wick and shell, which is calculated to be 182.16 W/K [37–39]. The value of C_{evap} was calculated with FLUENT software as follows. Except heating surface and the interface with porous wick, all surfaces of shell were set as adiabatic surface. A heat load and a temperature were put on heating surface and wick interface respectively. Through simulation, the temperature of heating surface in steady condition can be read, and then we can calculate C_{evap}.

3. Numerical method

Although quadrilateral mesh is more economical and has lower false diffusion than triangular mesh, because of the present dynamic mesh model adopted at the interface, quadrilateral mesh is inappropriate in the porous area, including the wick zone. Therefore quadrilateral mesh is adopted only in the shell, liquid grooves and vapor grooves, and triangular mesh used for the wick area. Fig. 2 shows the grid distribution for a symmetric half of the evaporator, generated by the commercial software package Gambit 2.3.16. Since both energy and flow equations are applied to the porous wick, while the solid shell and the groove only have energy transport, the grids in the fluid area are more concentrated than those in the solid zones. Furthermore, a steep pressure gradient could be predictable near the interface, and in order to get a smooth interface, the grids are generated in higher density there.

Because the objective of the paper is to investigate the influence of non-uniform heat load, both the geometric model and working conditions are modified to isolate the effect. Therefore, no previous experimental or simulation results can be used to compare with our simulation results. There are 99,498 triangular cells and 27,608 quadrilateral cells depicted in the model. From comparisons of trial results with different cell number models, this number of cells is enough to arrive at grid independence. More cells would increase more simulation time, but with little improvement in accuracy.

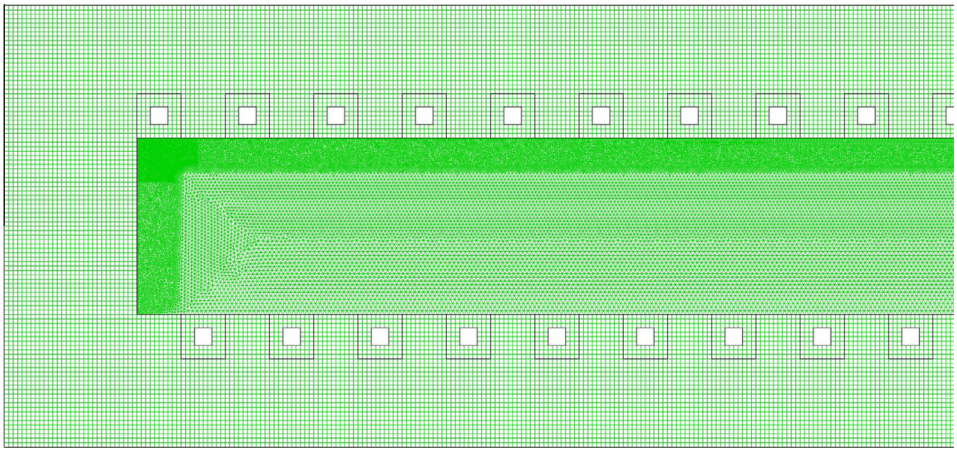

Fig. 2. Grid distribution of the geometric model.

4. Computational procedure

A general purpose CFD program FLUENT 14.0 within the commercial software ANSYS 14.0 is chosen for the computation because of its remarkable performance in dynamic mesh and numerical simulation for fluid flow and heat transfer. Since the dynamic mesh here needs a transient numerical simulation, the solver is set in the pressure-based transient option, the pressure-implicit with splitting of operators (PIOS) pressure–velocity coupling scheme used, because of its good convergence performance in transient models. A first order upwind and a second order upwind treatment are selected for momentum and energy spatial discretization respectively. Low relaxation factors in energy, pressure and momentum are used to ensure that the iteration will converge. The iterations were continued until the relative error in the mass conservation equation was below 5×10^{-4} and in the energy equation 1×10^{-7}. In addition, the temperature and velocity distributions of the model with the same working condition but with three different mesh systems (65,548, 127106, 203,534) were compared. Simulation results indicated that the computational errors of temperature distribution and velocity distribution using the two mesh systems (127,106, 203,534) are both less than 3%, so we can conclude that we can get a grid-independent simulation results using the mesh system (127,106 cells: 99,498 triangular cells and 27,608 quadrilateral cells). We use dynamic mesh at the interface of gas and liquid phases. In cell zones of porous wick, both smoothing mesh method and remeshing method are adopted. The dynamic mesh model would be activated since phase changing begins and would be deactivated when the balance in Eq. (29) is achieved. The flow diagram of computational procedure is presented in Fig. 3.

It is noteworthy that the model is based on a reasonable assumption: the pore in the wick is filled with either only vapor or only liquid. Therefore the minimum movement of the interface is 0.025 mm which is also the pore diameter of porous wick.

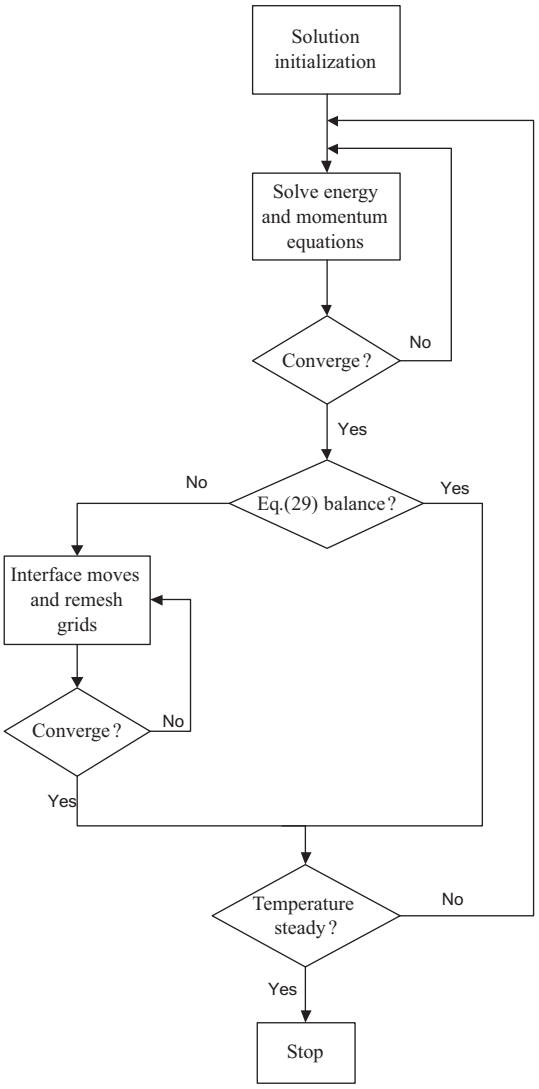

Fig. 3. Flow diagram of computational procedure.

5. Results and discussions

The selection of working fluids has great influence on the performance of LHP systems. They affect the working temperature [40,41] and the heat transfer coefficient, under different heat loads [42], because of variations in surface tension, latent heat and thermal conductivity [43]. In this work, methyl-alcohol is chosen as the working fluid, with the saturated pressure being 27,863 Pa at 308Porous medium is an important part in evaporators, since characteristics such as effective thermal conductivity, pore diameter, porosity and permeability can affect an evaporator's performance [10,14,17,44,45]. The thermal characteristics of working fluid are showed in Table 2. We use a steel porous wick with porosity 0.611 for our model. Working fluid and wick material are the same as those in Ref. [46].

Table 2
Working fluid thermal characteristics.

Methyl-alcohol (liquid)	
Density (kg m^{-3})	785
Specific Heat (J K^{-1} kg^{-1})	2534
Thermal conductivity (W m^{-1} K^{-1})	0.2022
Viscosity (kg m^{-1} s^{-1})	5.495×10^{-4}
Methyl-alcohol (vapor)	
Density (kg m^{-3})	1.43
Thermal conductivity (W m^{-1} K^{-1})	0.0163
Viscosity (kg m^{-1} s^{-1})	1.35×10^{-4}

In the simulation, several groups of heat load are adopted: the average heat fluxes (q_{load}) tested on the heating surface are 50,000 W/m^2, 60,000 W/m^2, 80,000 W/m^2, 100,000 W/m^2 and 120,000 W/m^2, and γ which represents heat concentration is set at zero (uniform heat load), 1, 2, 3 and 4. The operating pressure is 27863 Pa, and the shell material is steel.

5.1. Comparison on temperature distributions

Fig. 4 shows the temperature distributions under different concentrations with heat load q_{load} = 60,000 W/m^2 as well as the diagram of heat load distribution (Fig. 4(f)). From Fig. 4(a) and (b), a significant interface back off in the direction of positive x-axis can be seen in the side wall, and as heat concentration increases the phenomenon becomes less significant. It is the side metallic wall evaporation which could reduce evaporator heat transfer performance and be harmful to the operation of evaporators under extreme conditions. Because the effluence of vapor in sidewall is much less than those near the fins, even though the heat flux at the sidewall is much smaller, the vapor pressure is high enough to push back the interface. But this could have little influence on evaporative heat transfer coefficient because much less heat is conducted through the side wall. Furthermore, as heat concentration increases, there will be an interface retreat in the direction of negative y-axis near the fins. The high temperature region in Fig. 4 is also limited because the higher heat flux is loaded onto a smaller area.

Fig. 5 shows the interface position and the temperature distribution under the same heat concentration γ when the heat load increases as well as the diagram of heat load distribution (Fig. 5(f)). Because the heat flux increases, vapor flow will increase. Therefore, in some region that has no significant interface retreat in low heat load will also show a retreat of interface. On the other hand, for the region already with significant interface retreat in low heat load, the retreat will be strengthened, because more vapor will lead to a higher pressure to repel the interface.

There are two significant changes when the heat load concentrates: (1) the vapor–liquid interface backs off, and (2) the evaporation is limited to a smaller region and the temperature of the shell connected with the region increases sharply. Both affect the evaporator performance.

As the liquid gives way to the vapor which has much lower thermal conductivity, the heat transfer from shell to interface will decrease sharply. On the other hand, because the heat load is concentrated in a smaller area (the region with retreated interface in Fig. 4(d) and (e) has a higher thermal resistance), the mean heat transfer coefficient of the evaporator will decrease even more.

However, the increase of shell temperature could affect in the opposite way. Since the vapor flow will be channeled to specific grooves connected with high temperature shell while the heat load concentrates, more heat will be brought away as the vapor flows out. Therefore, the evaporator could perform better in heat transfer. Thus, the influence of non-uniform heat load on H_{evap} is rather complicated.

5.2. Comparison on working fluid velocity distribution

Fig. 6 shows the velocity distribution of vapor and liquid under different concentration when q_{load} = 60,000 W/m^2. When heat loads concentrate, vapor is gathered in several grooves which have higher heat flux. At the same time, the vapor velocity in highly heated grooves is increasing and other grooves' vapor velocity decreases. What is more, with reference to Fig. 4, working fluid gathered around high temperature fins.

It is noteworthy that some part of two-phase interface (the point in Fig. 7) seems connected to the shell. But in fact there is a narrow space (normally 0.025 mm to 0.1 mm) between the interface and the shell. Fig. 7 shows a more detailed velocity distribution in the region near the left two vapor grooves.

5.3. Comparison on outflow working fluid temperatures

Fig. 8 shows the influence of heat load on mass-weighted outflow working fluid temperature which represents the amount of energy being brought away with the outflow. In other words, under the same q_{load}, the higher the outflow temperature the more energy will be transferred to the vapor, and therefore an increase in convection heat transfer and improvement to H_{evap}.

For relative lower heat loads (50,000 W/m^2, 60,000 W/m^2 and 80,000 W/m^2), as heat flux concentrates, the outflow temperature increases sharply. That is because the concentrated heat flux gathers vapor flow into grooves whose temperatures have been raised at the same time. The two factors that could facilitate heat transfer between fluid and shell are: (1) since vapor flow is concentrated in several grooves, the flow velocity will increase too, leading to a higher convection heat transfer coefficient, and (2) groove temperature has been raised while the temperature of generated vapor in the interface can be regarded as constant. Thus the effective heat transfer area is decreased when heat concentrated and hence i the convection heat transfer coefficient is increased to some extent.

However, for higher heat loads (100,000 W/m^2 and 120,000 W/m^2), the curves are a little different in high heat concentration: the increase seems less. That is because heat flux concentration will lead to the retreat of interface which will result in a lower thermal conductance from shell to interface. And the lower heat transfer coefficient will prevent heat conduction to interface from high heat concentration region. Therefore a part of the heat must be conducted to the grooves and fins nearby. In other words, interface movement prevents the decrease of effective heat transfer area to some extent. All of these will make the factors (1) and (2) mentioned above less significant. Therefore the increase of convection heat transfer is impeded in highly concentrated heat loads.

For the last data point in at line 120,000 W/m^2 with γ being 3, it is lower than that in line 100,000 W/m^2 at the same γ. This is because the amount of vapor flow will increase with increasing heat load, and from what is mentioned earlier, — the vapor would not be heated so much under highly concentrated heat flux with retreated interface, outflow temperature can be lower than those under lower heat load under the same concentration condition.

5.4. Comparison on the position of vapor and liquid interface

Fig. 9 presents the relationship between interface position and different heat loads. Since the interface is an arc, as seen in Figs. 4 and 5, we adopted minimum y-coordinate of the interface to represent the position of interface.

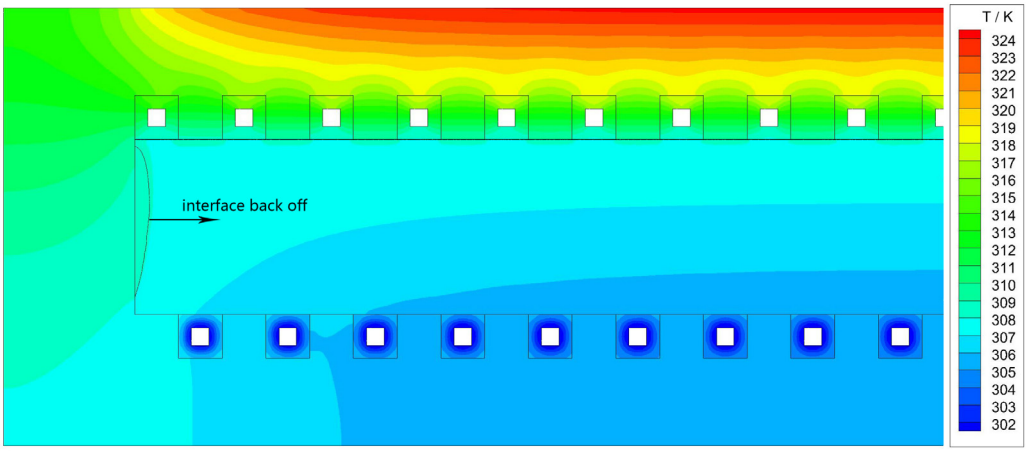

(a) $\gamma = 0$

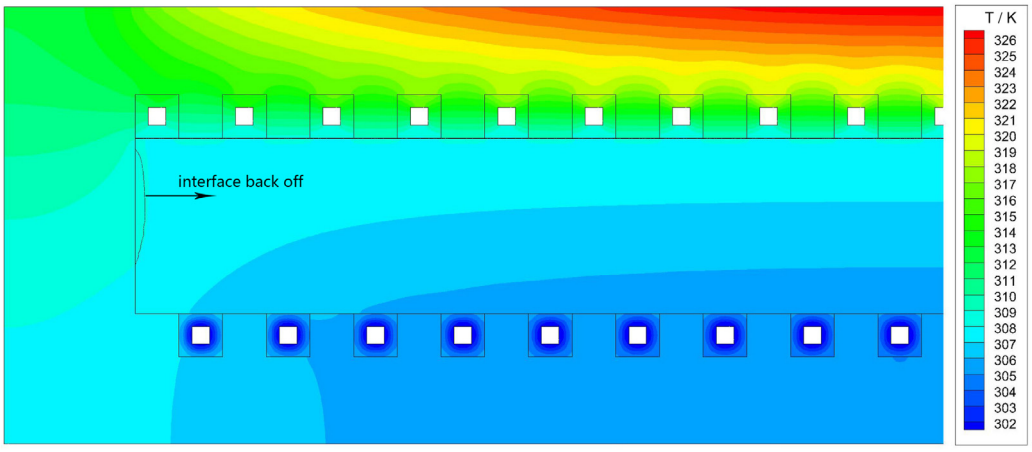

(b) $\gamma = 1$

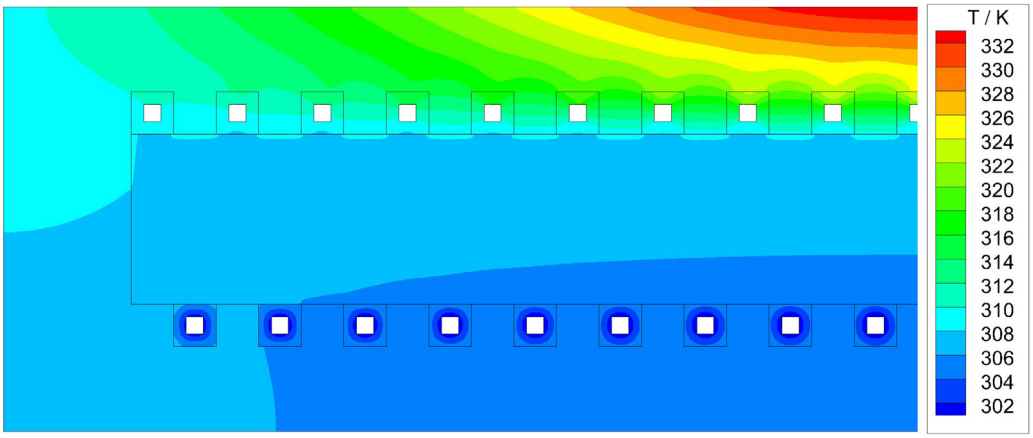

(c) $\gamma = 2$

Fig. 4. Temperature contours under different concentrations with heat load (q_{load}) 60000 W/m^2 and supplied heat load distribution.

What is more, because the oscillation of the evaporator in operation and the simulation in this paper, even when surface temperature is steady, the position of interface still oscillates. That is because interface will become steady only when Eq. (29) is balance. And due to the liquid flow speed is very low (normally 10^{-5} m/s), the pressure difference of liquid zone in wick can be neglected comparing with vapor-side. It means that a steady interface requires the pressure of vapor zone to be uniform. But in operation vapor must flow, and it will leads to pressure difference in vapor zone. Hence the interface will moves so that affect the vapor flow and pressure; and then interface moves again. Therefore two phase interface will oscillate in a very small amplitude.

Because of the oscillation, Fig. 9 shows the average minimum interface y-coordinates of several data points in the simulation

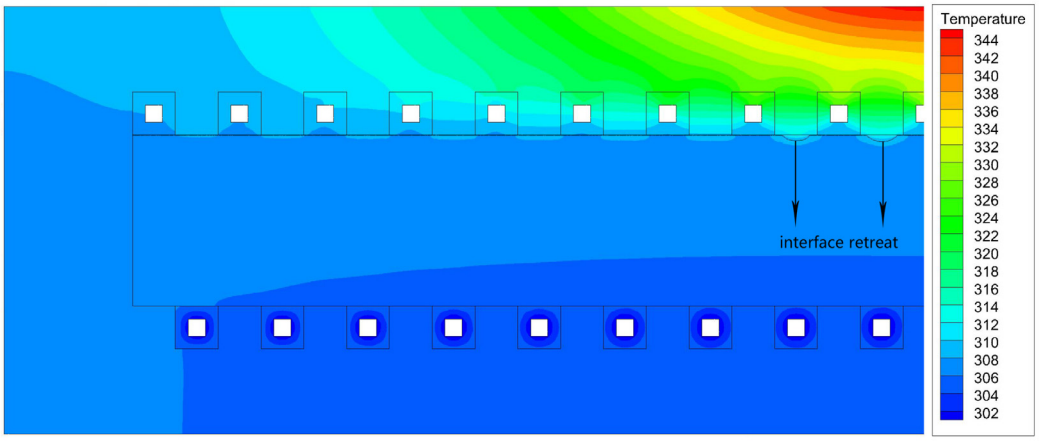

(d) $\gamma = 3$

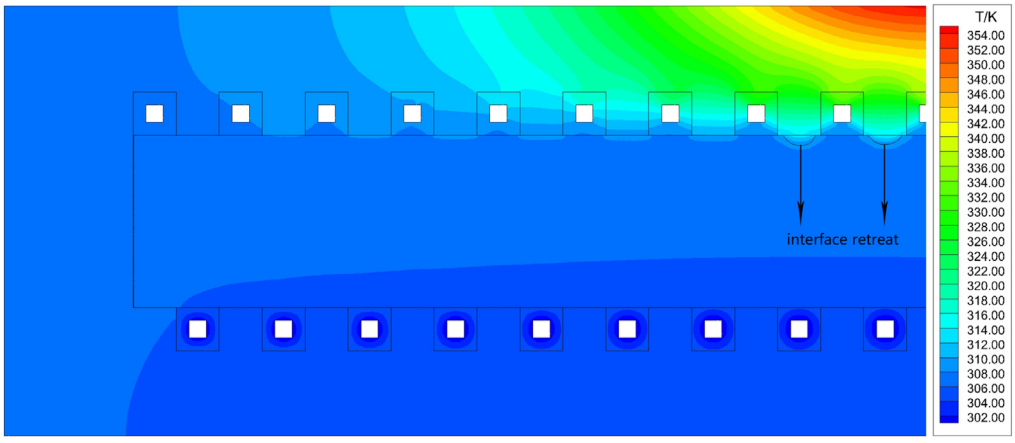

(e) $\gamma = 4$

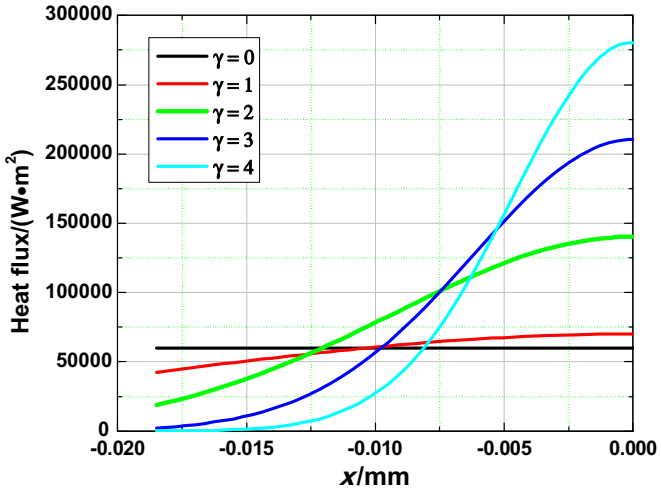

Fig. 4 (*continued*)

after it reached steady. The original y-coordinate of the interface is 2 mm, where the shell connects with the porous medium. A smaller y-coordinate means the vapor zone is deeper into the porous medium and will increase the evaporative heat transfer coefficient (H_{evap}) significantly, as the thermal resistance of the vapor zone is much larger than the same size liquid zone.

The result is similar to that of Figus and Bray [17]. Under relatively low heat load conditions, which means with the heat load being 50,000 W/m^2, 60,000 W/m^2 and 80,000 W/m^2, only after the concentration of heat exceeds a certain value will the interface retreat (in the direction of negative y-axis) significantly and the vapor zone will be deeper into the porous medium. As for higher heat loads (10,0000 W/m^2 and 120,000 W/m^2), it can be inferred from the figure that even for uniform heat load, at the lowest concentration condition, the heat flux is high enough for a significant retreat of the interface.

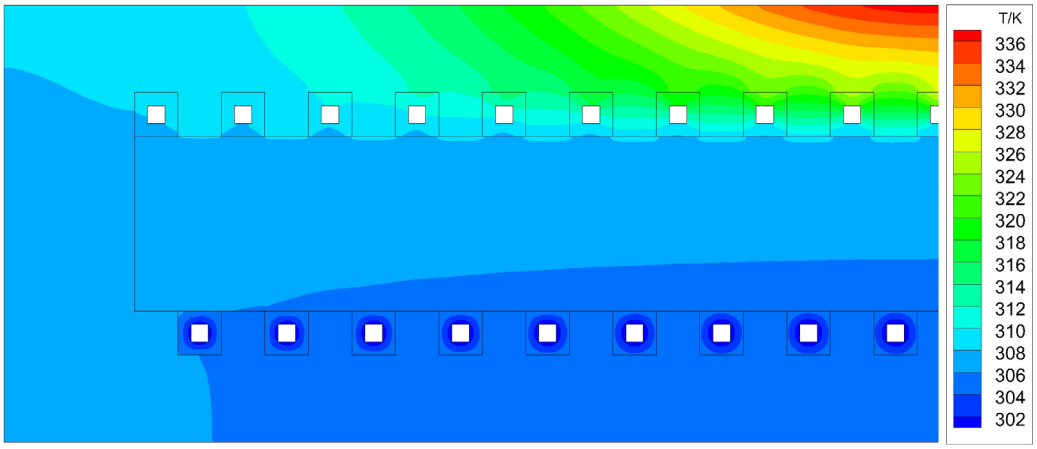

(a) $q_{load} = 50000\ \mathrm{W/m^2}$

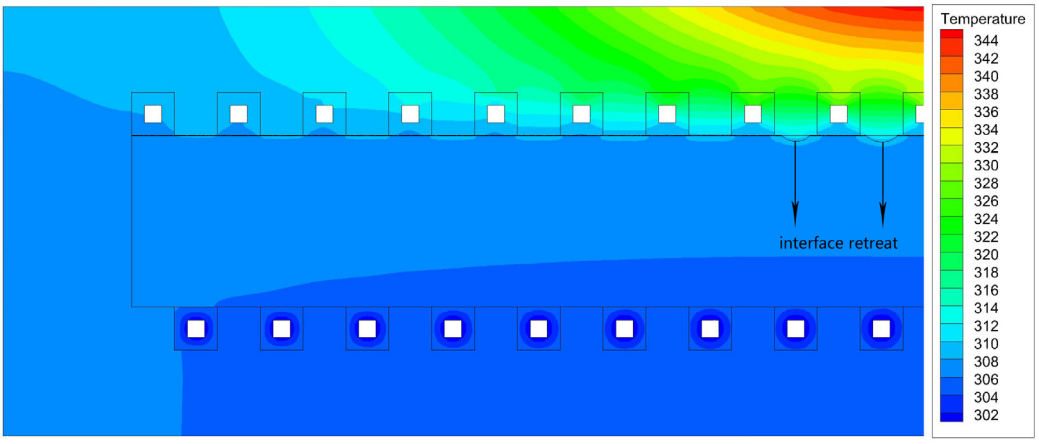

(b) $q_{load} = 60000\ \mathrm{W/m^2}$

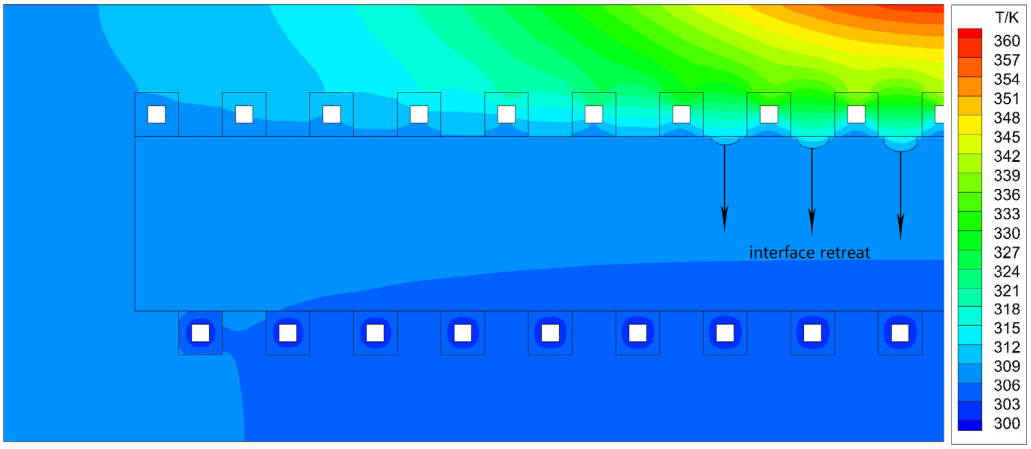

(c) $q_{load} = 80000\ \mathrm{W/m^2}$

Fig. 5. Temperature contours under different heat load (q_{load}) when $\gamma = 3$ and supplied heat load distribution.

5.5. Comparison on evaporative heat transfer coefficient

Fig. 10 displays the evaporative heat transfer coefficient (H_{evap}) with different heat flux and concentration. Above all, comparing the points under different heat flux but at the same heat concentration (γ), the lower the heat load, the higher H_{evap} will be. And there is a significant change in H_{evap} when the heat flux is concentrated, at 17.41%, 18.96%, 38.41% and 58.58% variance for 50.000 W/m^2, 60,000 W/m^2, 80,000 W/m^2 and 100,000 W/m^2, respectively.

From the analysis in 3.2 and 3.3, there are two key influencing factors that affect evaporative heat transfer: (1) vapor flow convection heat transfer, and (2) conduction heat transfer from shell to interface.

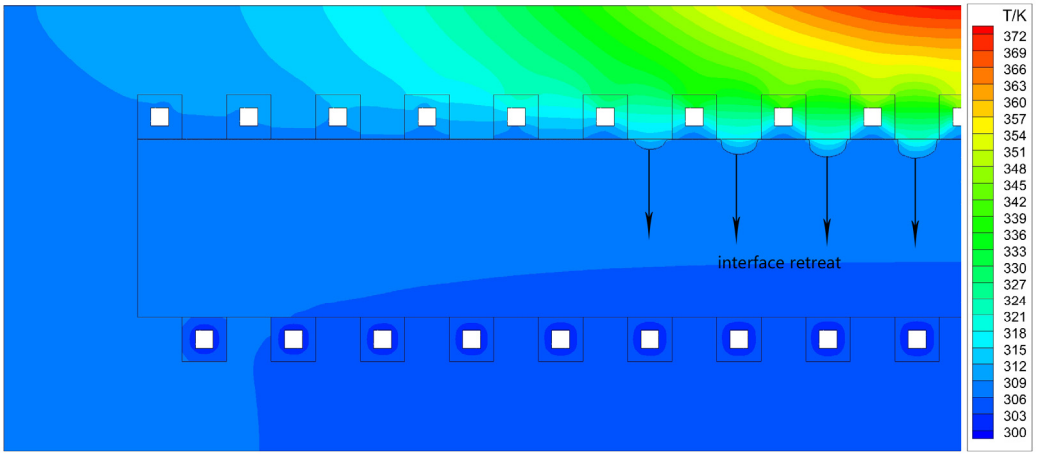

(d) q_{load} = 100000 W/m^2

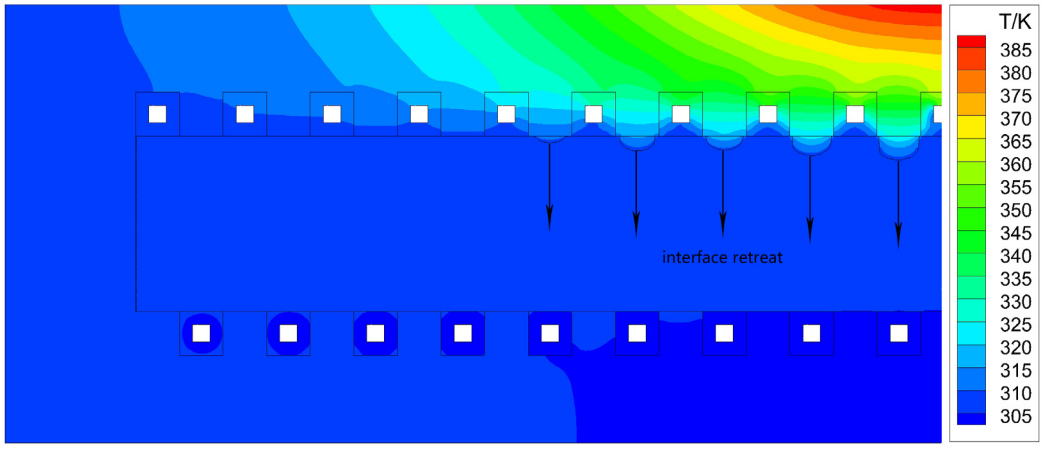

(e) q_{load} = 120,000 W/m^2

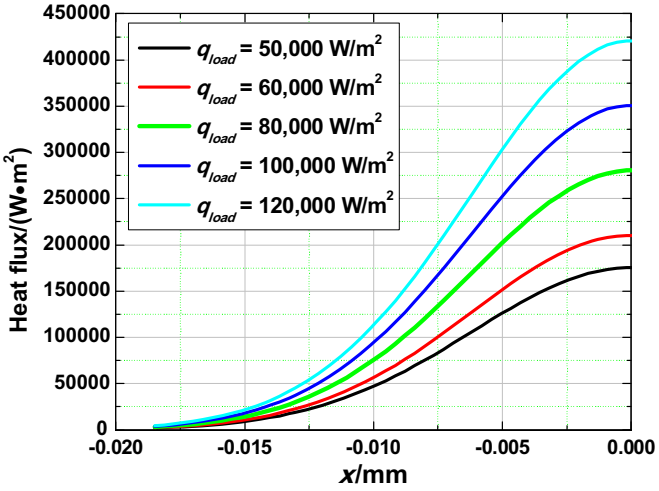

(f) Supplied heat load distribution

Fig. 5 (*continued*)

There is a peak at 50,000 W/m^2, 60,000 W/m^2 and 80,000 W/m^2. That is because before the peak, there is significant interface retreat so that the above factor (2) remains the valid, while the vapor flow convection heat transfer is strengthened when heat load increases. After the peak, interface retreat leading to a larger vapor zone will be significant because of the high flux. And therefore the conduction thermal resistance from shell to interface is increased. Although the convection heat transfer coefficient increases, apparently factor (2) has more influence on the H_{evap}. For 100,000 W/m^2 and 120,000 W/m^2, the evaporative heat transfer coefficient keeps decreasing because even in the lowest heat concentration there is significant interface retreat, like those

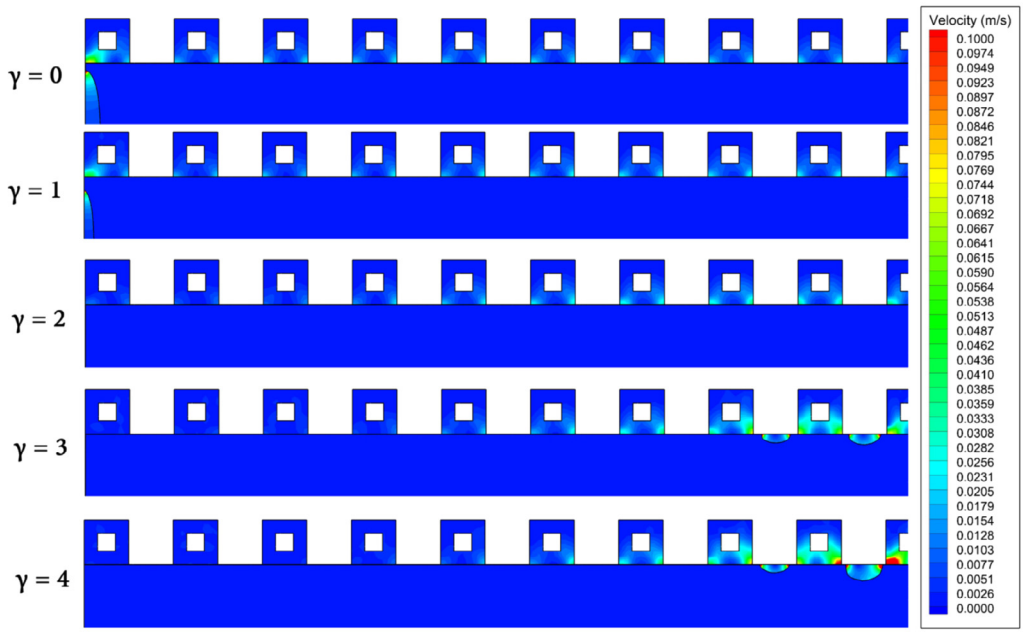

(a) Vapor velocity distribution under different concentration

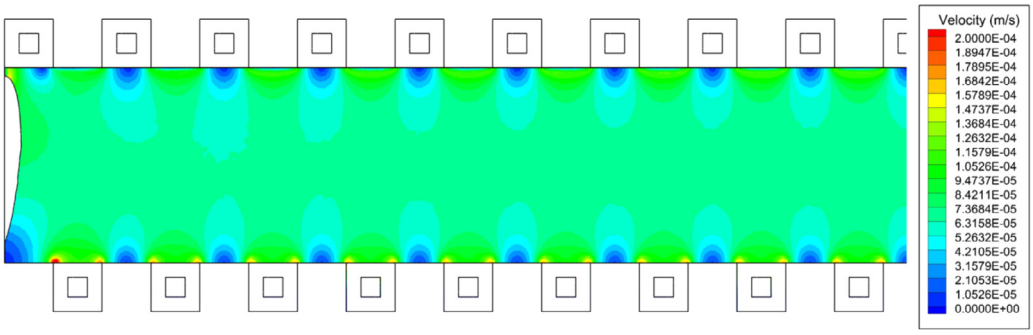

(b) Liquid velocity distribution, $\gamma = 0$

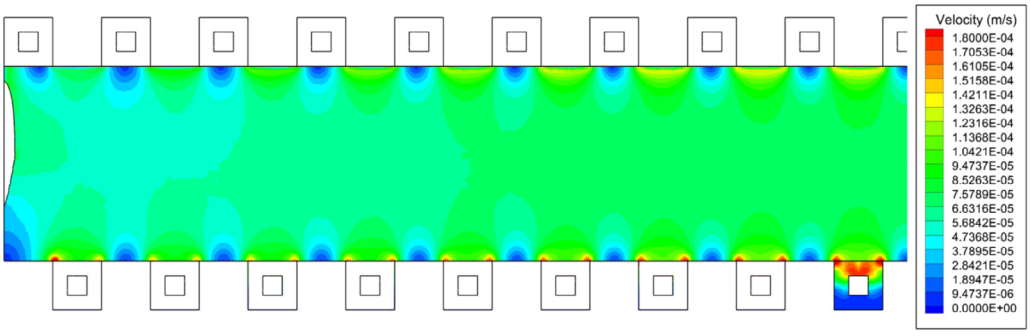

(c) Liquid velocity distribution, $\gamma = 1$

Fig. 6. Working fluid velocity distribution under different concentration when q_{load} = 60,000 W/m^2.

points after the peaks at lines of 50,000 W/m^2, 60,000 W/m^2 and 80,000 W/m^2.

However, obviously, the 120,000 W/m^2 line displays an interesting phenomenon that H_{evap} is much slower than any other point with the same concentration. It also has no peak. But it can be inferred from the regular pattern of the other line that the conditions of the evaporator under 120,000 W/m^2 are similar to those points after the peak in other lines. That means H_{evap} varies significantly with different heat load (just like points with $\gamma = 2$ in lines of 50,000, 60,000 and 80,000 W/m^2). Thus, H_{evap} at 120,000 W/m^2 could reasonably be lower.

5.6. Comparison on the maximum temperature of heating surface under different heat loads

Apart from the evaporative heat transfer coefficient, the maximum heating surface temperature is also an important factor in evaporator operation. Usually electronic components can still func-

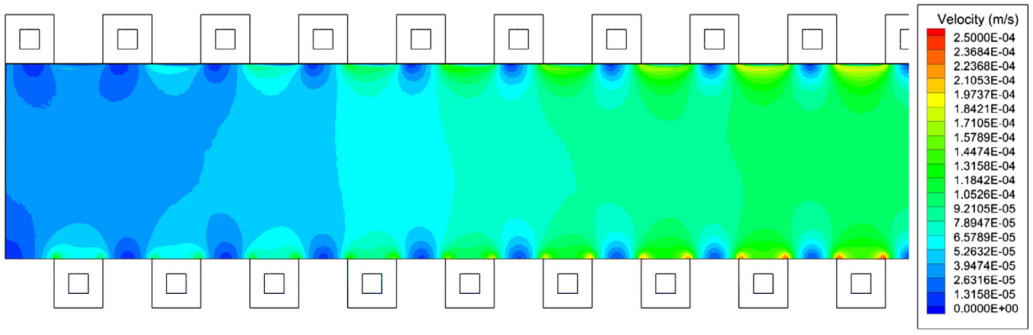

(d) Liquid velocity distribution, $\gamma = 2$

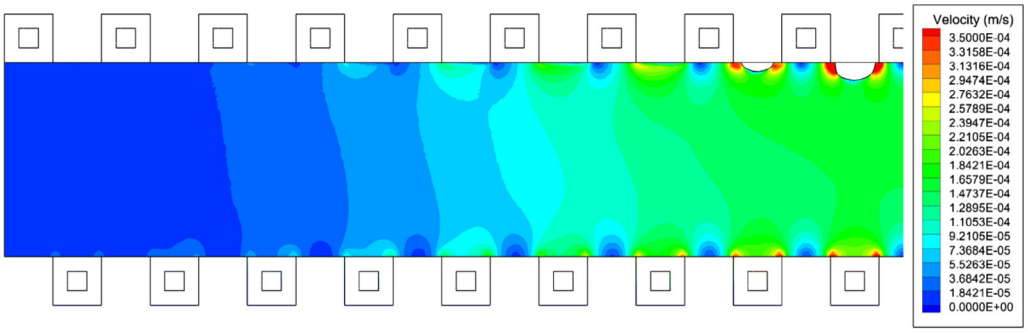

(e) Liquid velocity distribution, $\gamma = 3$

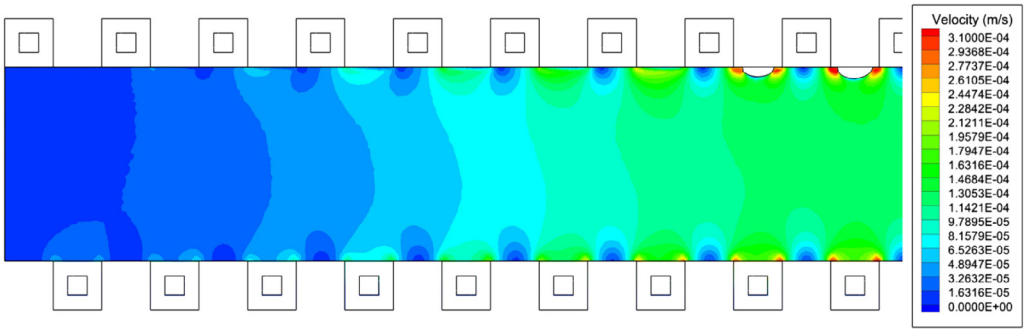

(f) Liquid velocity distribution, $\gamma = 4$

Fig. 6 (*continued*)

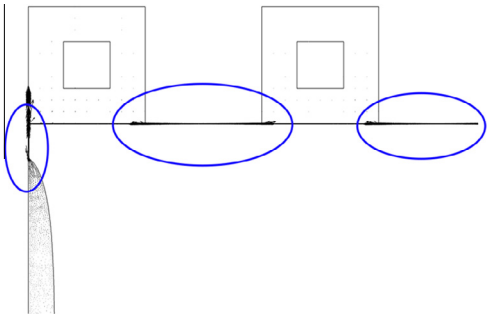

Fig. 7. Vapor velocity vector distribution when q_{load} = 60,000 W/m^2 and γ = 4.

tion in the temperature as high as 370 K. However, once the operation temperature exceeds 390 K, most electronic components will be out of action.

Fig. 11 displays the maximum temperature on the heating surface under different heat loads. There is a uniform tendency that as heat flux concentrates the maximum surface temperature

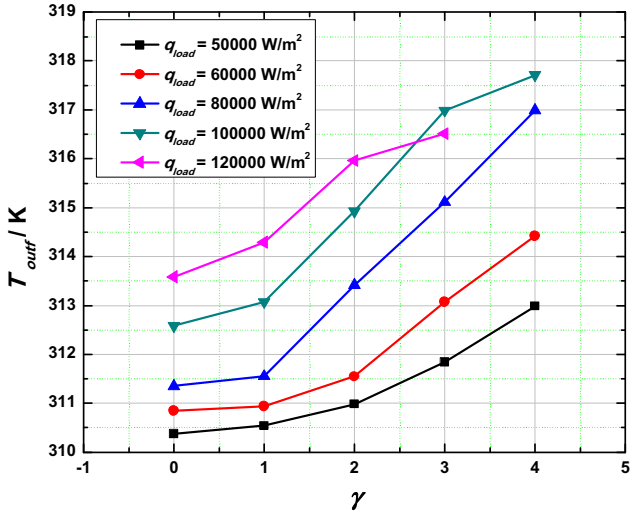

Fig. 8. Mass-weighted outflow temperature under different heat load conditions.

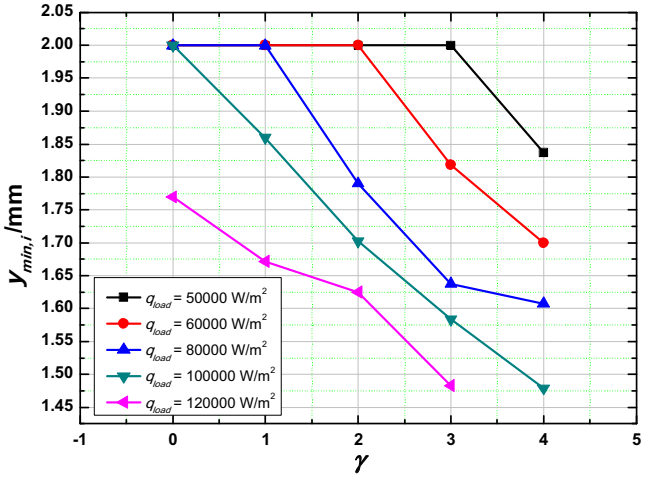

Fig. 9. General minimum node Y-coordinate of vapor and liquid interface under different heat loads.

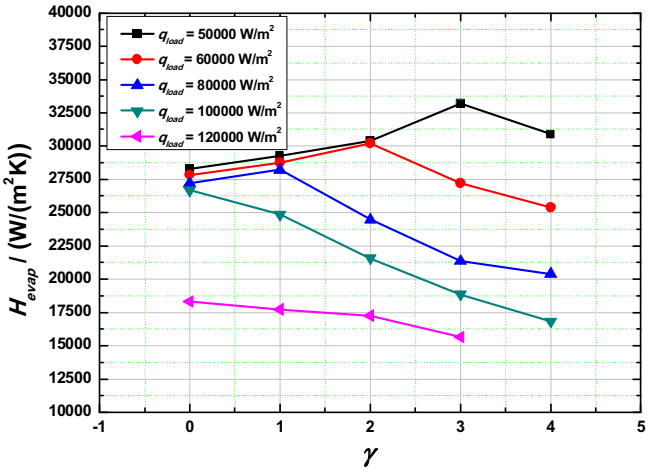

Fig. 10. Evaporative heat transfer coefficient (H_{evap}) under different average heat flux with different concentration.

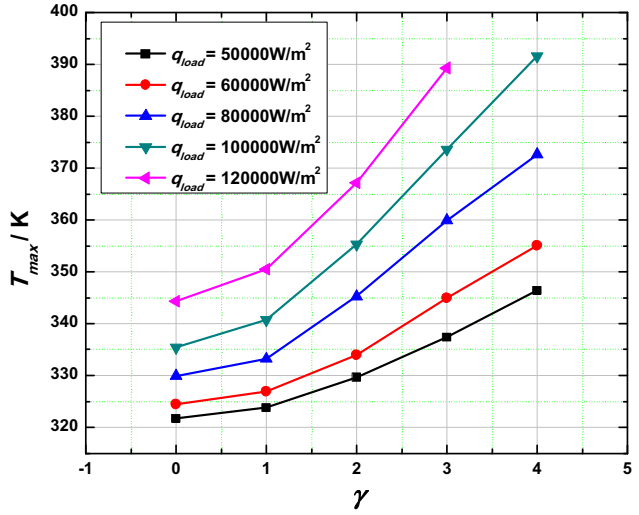

Fig. 11. Maximum heating surface temperature under different heat load conditions, with steel shell.

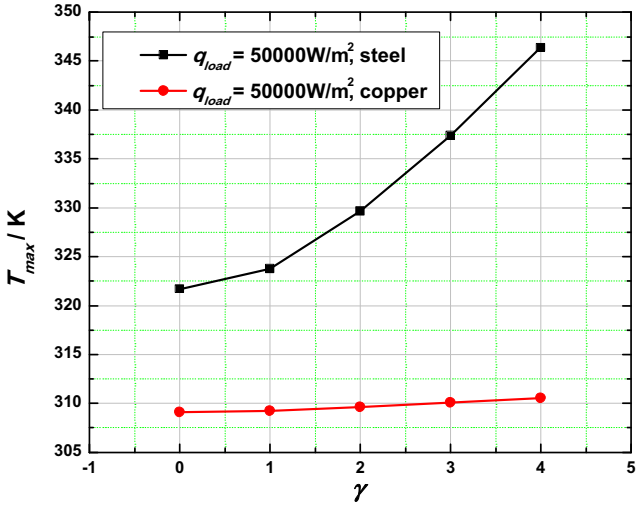

Fig. 12. Maximum heating surface temperature with different shell materials.

increases sharply. For extremely concentrated and high heat flux, the surface temperature could exceed 390 K which can be detrimental to the operation of electronic components.

Fortunately, similar phenomenon can be mitigated by the selection of relative high thermal conductivity shell material. Fig. 12 shows the maximum temperature on heating surface under 50,000 W/m^2 with different shell material, steel and copper. The thermal conductivity of copper is more than 20 times that of steel, so that the surface temperature will be much lower than that with steel shell. The maximum superheat (the maximum shell temperature minus inflow temperature) of steel shell and copper shell is 38.39 K. and 2.52 K which is reduced by 93.4% through using copper material. Therefore, unless under extreme high and concentrated heat loads, the maximum heating surface temperature of evaporator in operation can be limited in an acceptable range by choosing a high thermal conductivity material.

This simulation was carried out for a steel wick, steel evaporator body and methyl-alcohol as a working fluid according to Wan et al. [46], the basic results and conclusions of this work will not be affected significantly by the combination of different materials. But it should be noted that, according to the data from Reay and Kew [47], the combination of steel and methyl-alcohol is incompatible for heat pipes and loop heat pipes by reason of generation of non-condensable gases inside these devices. In future work, both numerically investigation and experimental research of a heat pipe, we will consider using the compatible materials.

6. Conclusions

In this paper, detailed numerical simulations by using a dynamic mesh model using the commercial software FLUENT 14.0 have been conducted, in order to investigate the influence of various concentrated heat loads on the performance of the evaporator in HLPs. The evaporation heat transfer coefficient, interface position, outflow temperature as well as maximum surface temperature are presented and analyzed. Furthermore, a series of simulations of different shell material evaporators has been presented to investigate a possible way to reduce maximum surface temperature in operation.

The influence of heat concentration on evaporator performance is rather complicated and conclusions are:

(1) The concentration of heat load will help heat convection and lead to interface retreat some time. Therefore when the heat load is not highly concentrated and heat flux is relative low,

non-uniform heat facilitates the heat transfer. On the other hand, it will decrease heat transfer when operating under extreme concentrated or high heat loads.

(2) The maximum temperature on the heating surface will increase sharply when heat flux is concentrated and can be detrimental to the operation of some electronic components under extreme high heat flux. But the temperature can be reduced through choosing a high thermal conductivity shell material.

In conclusion, the possibility of heat concentration should be considered when choosing and designing HLP evaporators for different operation conditions.

Acknowledgements

This research was supported by the National Natural Science Foundation of China (51106060 and 51106057) and the Natural Science Foundation of Hubei Province, China (2012FFB02214).

References

[1] F.J. Stenger, Experimental feasibility study of water-filled-capillary-pumped heat transfer loops, Tech. Rep. NASA TM-X-1310, NASA Lewis Research Center, Cleve-land, OH, 1966.
[2] Y.F. Maidanik, S. Vershinin, V. Kholdov, J. Dolgirev, Heat Transfer Apparatus, US Patent No. 4515209, 1985.
[3] D.R. Chalmers, J.J. Pustay, C.B. Moy, E.J. Kroliczeck, Application of capillary pumped loop heat transport systems to large spacecraft, AIAA Paper 86–1295, 1986.
[4] R. Singh, A. Akbarzadeh, C. Dixon, M. Mochizuki, R.R. Riehl, Miniature loop heat pipe with flat evaporator for cooling computer CPU, IEEE Trans. Compon. Packag. Technol. 30 (1) (2007) 42–49.
[5] J. Ku, Operating Characteristics of Loop Heat Pipes, SAE paper 1999-01-2007, 1999.
[6] A.A. Adoni, A. Ambirajan, V.S. Jasvanth, D. Kumar, P. Dutta, Theoretical and experimental studies on an ammonia-based loop heat pipe with a flat evaporator, IEEE Trans. Compon. Packag. Technol. 33 (2) (2010) 478–487.
[7] V.M. Kiseev, V.V. Vlassov, I. Murakoa, Experimental optimization of capillary structure for loop heat pipes and heat switches, Appl. Therm. Eng. 30 (11–12) (2010) 1312–1319.
[8] W. Joung, T. Yu, J. Lee, Experimental study on the operating characteristics of a flat bifacial evaporator loop heat pipe, Int. J. Heat Mass Transf. 53 (1–3) (2010) 276–285.
[9] K.S. Udell, Heat transfer in porous media heated from above with evaporation, condensation, and capillary effects, J. Heat Transfer 105 (1983) 485–492.
[10] T.S. Zhao, Q. Liao, On capillary-driven flow and phase-change heat transfer in a porous structure heated by a finned surface: measurements and modeling, Int. J. Heat Mass Transf. 43 (7) (2000) 1141–1155.
[11] J. Ku, High frequency low amplitude temperature oscillations in loop heat pipe operation, in: International Conference on Environmental Systems, Vancouver, July 2003 (SAE paper 2003-01-2387), pp. 9.
[12] J. Ku, J.I. Rodriguez, Low frequency high amplitude temperature oscillations in loop heat pipe operation, in: International Conference on Environmental Systems, Vancouver, July 2003 (SAE paper 2003-01-2386), pp. 12.
[13] Y. Chen, M. Groll, R. Mertz, Y.F. Maydanik, S.V. Vershinin, Steady-state and transient performance of a miniature loop heat pipe, Int. J. Therm. Sci. 45 (11) (2006) 1084–1090.
[14] Y. Cao, A. Faghri, Conjugate analysis of a flat-plate type evaporator for capillary pumped loops with three-dimensional vapor flow in groove, Int. J. Heat Mass Transf. 37 (3) (1994) 401–409.
[15] Y. Cao, A. Faghri, Analytical solutions of flow and heat transfer in a porous structure with partial heating and evaporation on the upper surface, Int. J. Heat Mass Transf. 37 (10) (1994) 1525–1553.
[16] A.S. Demidov, E.S. Yatsenko, Investigation of heat and mass transfer in the evaporation zone of a heat pipe operating by the inverted meniscus principle, Int. J. Heat Mass Transf. 37 (14) (1944) 2155–2163.
[17] C. Figus, Y. Le Bray, S. Bories, M. Prat, Heat and mass transfer with phase change in a porous structure partially heated: continuum model and pore network simulations, Int. J. Heat Mass Transf. 42 (14) (1999) 2557–2569.
[18] J. Xu, Y. Zou, M. Fan, L. Cheng, Effect of pore parameters on thermal conductivity of sintered LHP wicks, Int. J. Heat Mass Transf. 55 (2012) 2702–2706.
[19] S.C. Wu, C.J. Huang, S.H. Chen, Y.M. Chen, Manufacturing and testing of the double-layer wick structure in a loop heat pipe, Int. J. Heat Mass Transf. 56 (2013) 709–714.
[20] F.C. Lin, B.H. Liu, C.T. Huang, Y.M. Chen, Int. J. Heat Mass Transf. 54 (2011) 4621–4629.
[21] G. Xin, K. Cui, Y. Zou, L. Cheng, Reduction of effective thermal conductivity for sintered LHP wicks, Int. J. Heat Mass Transf. 53 (2010) 2932–2934.
[22] D. Deng, Y. Tang, G. Huang, L. Lu, D. Yuan, Characterization of capillary performance of composite wicks for two-phase heat transfer devices, Int. J. Heat Mass Transf. 56 (2013) 283–293.
[23] J. Xu, L. Zhang, H. Xu, Performance of LHPs with a novel design evaporator, Int. J. Heat Mass Transf. 55 (2012) 7005–7014.
[24] X.H. Nguyen, B.H. Sung, J. Choi, S.R. Ryoo, H.S. Ko, C. Kim, Study on heat transfer performance for loop heat pipe with circular flat evaporator, Int. J. Heat Mass Transf. 55 (2012) 1304–1315.
[25] V.M. Kiseev, V.V. Vlassov, I. Muraoka, Optimization of capillary structures for inverted meniscus evaporators of loop heat pipes and heat switches, Int. J. Heat Mass Transf. 53 (2010) 2143–2148.
[26] Y. Chen, F. Yao, M. Shi, Thermal response of a heat pipe with axially "X"-shaped microgrooves, Int. J. Heat Mass Transf. 55 (2012) 4476–4484.
[27] G. Lin, N. Li, L. Bai, D. Wen, Experimental investigation of a dual compensation chamber loop heat pipe, Int. J. Heat Mass Transf. 53 (2010) 3231–3240.
[28] Y. Zhao, T. Yan, J. Liang, Experimental study on a cryogenic loop heat pipe with high heat capacity, Int. J. Heat Mass Transf. 54 (2011) 3304–3308.
[29] L. Bai, G. Lin, H. Zhang, J. Miao, D. We, Effect of component layout on the operation of a miniature cryogenic loop heat pipe, Int. J. Heat Mass Transf. 60 (2013) 61–68.
[30] I. Muraoka, F.M. Ramos, V.V. Vlassov, Experimental and theoretical investigation of a capillary pumped loop with a porous element in the condenser, Int. Commun. Heat Mass Transfer 5 (8) (1998) 1085–1094.
[31] Z.M. Wan, W. Liu, L. Zhang, T.Z. Ming, Investigation of small-scale flat-plate type capillary pumped loop for high heat flux applications, Chinese Space Science and Technology 6 (2007) 19–24.
[32] Z.M. Wan, W. Liu, D.X. Gai, Z.C. Liu, Numerical simulation of heat transfer with phase change in small-scale flat capillary pumped loop finned evaporator, Journal of Chemical Industry and Engineering (China) 58 (2007) 2994–3000.
[33] A.A. Adoni, A. Ambirajan, V.S. Jasvanth, D. Kumar, P. Dutta, K. Srinivasan, Thermohydraulic modeling of capillary pumped loop and loop heat pipe, J. Thermophys. Heat Transfer 21 (2) (2007) 410–421.
[34] Fluent, ANSYS FLUENT 12.0 User's Guide, April 2009.
[35] P.Y.A. Chuang, An improved steady-state model of loop heat pipes based on experimental and theoretical analyses, Ph.D. thesis, The Pennsylvania State University, 2003.
[36] A.A. Adoni, V.S. Jasvanth, A. Ambirajan, D. Kumar, K. Badarinarayana, D.R. Bhandari, P. Dutta, Evaporation heat transfer coefficient in a capillary pumped loop for different working fluids, Heat Transfer Eng. 33 (9) (2012) 765–774.
[37] M.T. North, D.B. Sarraf, J. H. Rosenfeld, Y.F. Maidanik, S. Vershinin, High heat flux loop heat pipes, in: Proceedings of the 6th European Symposium on Space Environmental Control Systems (ESA SP-400), vol. 1, 1997, pp. 371–376.
[38] Y.F. Maydanik, S.V. Vershinin, Development and tests of ammonia miniature loop heat pipes with cylindrical evaporators, Appl. Therm. Eng. 29 (11–12) (2009) 2297–2301.
[39] R. Singh, A. Akbarzadeh, M. Mochizuki, Effect of wick characteristics on the thermal performance of the miniature loop heat pipe, J. Heat Transfer 131 (8) (2009) 08601-1–08601-10.
[40] J.H. Boo, W.B. Chung, Thermal performance of a small-scale loop heat pipe with PP wick, in: 13th IHPC, Shanghai, China, pp. 259–264, 21–25 September 2004.
[41] T. Kaya, J. Ku, A parametric study of performance characteristics of loop heat pipes, in: International Conference on Environmental Systems, Denver, July 1999, pp. 7 (SAE paper 1999-01-2006).
[42] J.I. Rodriguez, M. Pauken, Performance characterization and model verification of a loop heat pipe, in: International Conference on Environmental Systems, Toulouse, July 2000, pp. 7 (SAE paper 2000-01-2317).
[43] J. Baumann, S. Rawal, Viability of loop heat pipes for space solar power applications, in: AIAA Thermophysics Conference, 35th, Anaheim, CA, 11–14 June 2001, pp. 10 (AIAA 2001-3078).
[44] W. Yao, J. Miao, X. Shao, Parametric analysis on LHP/CPL evaporator performance and critical heat flux by two-dimensional calculation, in: 13th IHPC, Shanghai, China, 21–25 September 2004, pp. 125–132.
[45] V. Platel, O. Fudym, C. Butto, P. Briend, Coefficient de transfert, à l'in-terface de vaporisation, d'une boucle de fluide diphasique à pompage capillaire, Rev. Gén. Therm. 35 (1996) (1996) 592–598.
[46] J. Wan, Z.M. Wan, J. Liu, K. Su, H. Li, X.H. Hu, Investigation on startup characteristics of small-scale flat-plate type capillary pumped loop evaporator, Int. Conf. Comput. Appl. Syst. Model. 6 (2010) (2010) 63–66.
[47] D.A. Reay, P.A. Kew, Heat Pipe Theory Design and Applications, fifth edition., Butterworth-Heinemann, 2006.